STARDUST experimental campaign and numerical simulations: influence of obstacles and

temperature on dust resuspension in a vacuum vessel under LOVA

STARDUST experimental campaign and numerical simulations: influence of obstacles and temperature on dust resuspension in a vacuum vessel under LOVA

C. Bellecci[1], P. Gaudio[1], I. Lupelli[1], A. Malizia[1], M.T. Porfiri[2], R. Quaranta[1] and M. Richetta[1]

[1] Faculty of Engineering, University of Rome 'Tor Vergata', Via del Politecnico 1, 00133 Rome, Italy
[2] ENEA Nuclear Fusion Technologies, Via Enrico Fermi 45 I, 00044, Frascati, Italy

Abstract

Activated dust mobilization during a Loss of Vacuum Accident (LOVA) is one of the safety concerns for the International Thermonuclear Experimental Reactor (ITER). Intense thermal loads in fusion devices occur during plasma disruptions, edge localized modes and vertical displacement events. They will result in macroscopic erosion of the plasma facing materials and consequent accumulation of activated dust into the ITER vacuum vessel (VV). These kinds of events can cause dust leakage outside the VV that represents a high radiological risk for the workers and the population. A small facility, Small Tank for Aerosol Removal and Dust (STARDUST), was set up at the ENEA Frascati laboratories to perform experiments concerning the dust mobilization in a volume with the initial conditions similar to those existing in ITER VV. The aim of this work was to reproduce a low pressurization rate (300 Pa s^{-1}) LOVA event in a VV due to a small air leakage for two different positions of the leak, at the equatorial port level and at the divertor port level, in order to evaluate the influence of obstacles and walls temperature on dust resuspension during both maintenance (MC) and accident conditions (AC) ($T_{walls} = 25\,°C$ MC, $110\,°C$ AC). The dusts used were tungsten (W), stainless steel 316 (SS316) and carbon (C), similar to those produced inside the vacuum chamber in a fusion reactor when the plasma facing materials vaporize due to the high energy deposition. The experimental campaign has been carried out by introducing inside STARDUST facility an obstacle to simulate the presence of objects, such as divertor. In the obstacle a slit was cut to simulate the limiter–divertor gap inside ITER VV. In this paper experimental campaign results are shown in order to investigate how the divertor and limiter–divertor gap influence dust mobilization into a VV. A two-dimensional (2D) modelling of STARDUST was made using the CFD commercial code FLUENT, in order to get a preliminary overview of the fluid dynamics behaviour during a LOVA event and to justify the mobilization data. In addition, a numerical model was developed to compare numerical results with experimental ones.

(Some figures in this article are in colour only in the electronic version)

1. Premise

This work takes International Thermonuclear Experimental Reactor (ITER) as a reference machine because it is the most interesting project in the fusion safety field for its safety concerns and layout. Nevertheless, the results are not directly applicable to the international fusion reactor. The study was developed in the frame of the computer code validation for nuclear safety accident analysis. It is a starting point for dust mobilization investigation but it needs larger verification before being extrapolated to facilities bigger than STARDUST.

2. Introduction

Intense thermal loads in fusion devices occur during plasma disruptions, edge localized modes (ELMs) and vertical displacement events (VDEs). They will result in macroscopic erosion of the plasma facing materials and consequent

accumulation of activated dust in a vacuum vessel (VV). In ITER it is foreseen that the continuous first wall erosion caused by plasma disruptions and the bumps of the plasma during the operation induce the formation of mobilizable materials, in the shape of radioactive dust [1]. The safety limit for dust inside the ITER VV has been proposed to the safety authorities to be 1000 kg, without any precision on the composition. However, it is settled also a 'hot dust' limit (defined as the dust on surfaces with $T > 400\,^\circ C$) of 6 kg each of C, Be and W [2]. These administrative limits have been fixed to avoid, also in the case of severe accident, the evacuation of the population from the area surrounding the plant [2] because the consequent calculated releases should cause doses below the limits according to the current recommendations of the International Commission on Radiological Protection. In the case of Loss of Vacuum Accidents (LOVA) [3], air inlet occurs due to the pressure difference between the atmospheric condition and the internal condition. A LOVA event causes mobilization of the dust that can exit the VV, threatening public safety because it contains tritium, it is radioactive from activation products, and may be chemically reactive and/or toxic [1]. Several experiments with STARDUST facility have been conducted to reproduce a low pressurization rate (300 Pa s^{-1}) LOVA [3] event in ITER due to a small air leakage for two different positions of the leak, at the equatorial port level and at the divertor port level, in order to evaluate the influence of obstacles (such as the divertor and the limiter–divertor gap) and temperature on dust resuspension during both MC and AC. The pressurization rate of 300 Pa s^{-1} is the estimated consequence of a 0.02 m^2 wide breach during the first seconds of a LOVA, as defined by Generic Site Specific Report (GSSR) [4]. To support the experiments, simulations by means of Computational Fluid Dynamics (CFD) codes are considered an essential tool [5]. Therefore, experimental activities and numerical simulation campaigns have been carried out in strong correlation in order to understand the capabilities of these computational codes in predicting correctly the characteristics of turbulent flows. A two-dimensional (2D) modelling of STARDUST, made using the CFD commercial code FLUENT, has been carried out in order to get a preliminary overview of the fluid dynamics behaviour during a LOVA event. A comparison of the experiments performed in STARDUST with the numerical simulation results will be shown.

3. Experimental campaign

STARDUST [1, 6, 7] (figure 1) is a cylindrical facility designed to study the dust behaviour in a fusion plant when a LOVA occurs. It is a steel tank in which a loss of vacuum is simulated through the air inlet. At the beginning of the experiment the inside pressure of about 100 Pa was achieved. Afterwards air, adjusted to get a pressurization rate of 300 Pa s^{-1}, flows through either valve A or B. Valve A reproduces a small leak in a sealed window of the equatorial port and valve B simulates the leak at the divertor port level (figure 2).

3.1. New STARDUST experimental setup

In the past mobilization experiments have been performed at 110 °C with an empty tank. In the experimental campaign we
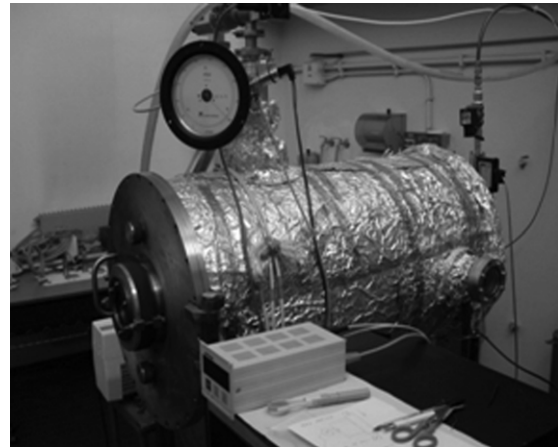

Figure 1. STARDUST Facility.

are dealing with the influence of an obstacle, and temperature on the dust mobilization is investigated.

Two different sets of measurements were performed: in the first one, in order to take into account the ITER VV wall temperatures under normal operation conditions, the external walls of STARDUST were heated up to 110 °C [4] (the nominal VV wall temperature is almost 120 °C during normal operation [8]) by electrical resistances; the second set represents the MC, during which an environmental temperature was set equal to 25 °C. In both cases, inside the chamber, dry conditions were maintained in order to consider the worst situation, as the entrainment ratio decreases in the case of high value of the relative humidity [9]. A data acquisition system allows us to control the pressure, the temperature of the walls and the air flow rate. Figure 3 shows a schematic layout of the LOVA simulation experiment made by STARDUST.

In ITER VV there are several structures that could influence the dust mobilization during a LOVA, such as the divertor cassettes (figure 4(*b*)). In order to estimate their effects an obstacle was placed into STARDUST. The obstacle is a stainless steel cot and it is provided with a bridge that aims to reproduce the divertor dome (figure 4(*a*)). After a first set of experiments, a slit on the obstacle has been made in order to analyse the effects of a gap if the air inlet occurs between the limiter and the divertor (LDG—limiter–divertor gap) in ITER by the comparison of dust mobilized in the experiments with and without the slit on the obstacle.

The main geometrical characteristics of the slit (dimensions in mm) are reported in figure 4(*c*), the height of the slit is 2.5 mm and the width is 290 mm.

The type of dust used (W, C, SS316) is similar to that found inside the vacuum chamber of a fusion facility, when the plasma facing materials vaporize for high energy deposition due to the disruptions [7]. Scanning electron microscope (SEM) analysis has been carried out for characterizing the commercial dust used for the experiments [7]. The dust mean diameters measured were 0.3–0.5 μm for W, 20–30 μm for SS316 and 4–5 μm for C. The dust size distributions are shown in figure 5 for C (received from FZK), in figure 6 for W (treated by carbon deposition, 2.0–3.0 nm) and in figure 7 for SS316 (treated by carbon deposition, 2.0–3.0 nm). The results
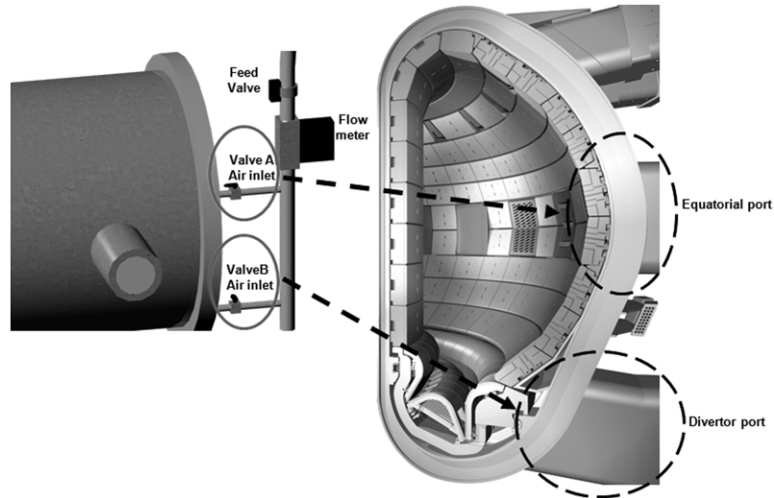
Figure 2. Valves A and B on STARDUST (on the left) that are used to reproduce, respectively, a LOVA at the equatorial and divertor port on ITER (on the right).
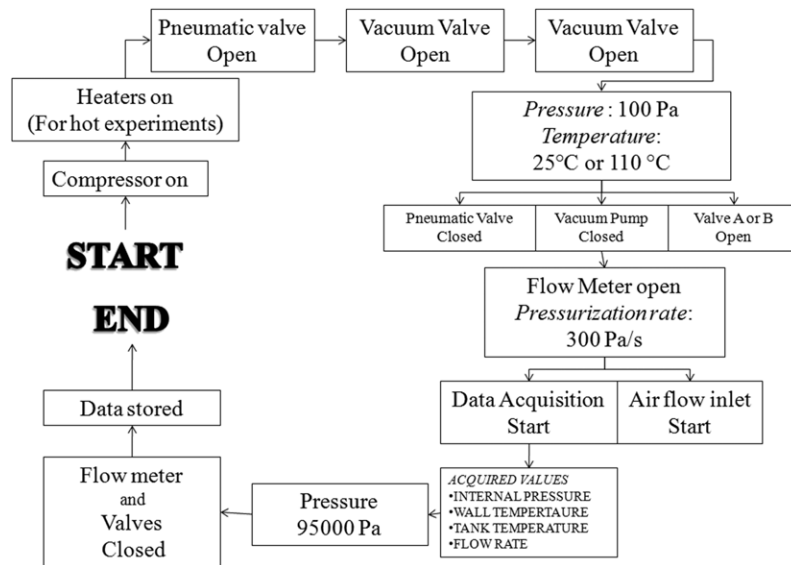

Figure 3. Experimental sequence for a Loss of Vacuum Accident simulation at STARDUST.

of the SEM scanning revealed a size distribution of the dust different from those declared by the commercial companies, that were 0.6–0.9 μm for W and 45 μm for SS316 against the 0.3–0.5 μm detected by the SEM for W and 15–30 μm for SS316, respectively [7].

Among the dust sizes commercially available, those similar to the dusts generated in the disruption phenomena have been chosen [7]. While the W and the C grains had the tendency to agglomerate with each other, the stainless steel, being of bigger size and with a high specific weight, remained well separated. This behaviour was significant in the piles preparation for the experiments, because it was possible to form similar heaps for all the tests with the stainless steel, while the tungsten piles and carbon piles were different for each test [7]. This feature has an influence on the mobilization rate. The effect of the humidity in the agglomeration has to be excluded, because of the vacuum condition in the tank [7]. The dust was placed on a tray (area 25 cm^2) in order to reproduce a superficial density as expected in ITER (figure 8). In these experiments the dust has been deposited on the tray using a sieve to avoid heaps.

The amounts of dust used were 0.5 g for W and SS316, 0.2 g for C. The experiments have been performed in the following configurations:

(a) Tray with dust (figure 9);
(b) Tray without the obstacle, in the bottom part of the tank (figure 9);
(c) Tray under the obstacle at the bottom part of the tank (figure 9);
(d) Tray inside the obstacle, under the bridge (figure 9);
(e) Tray inside the obstacle, on the bridge (figure 9).

Dust resuspended fraction is [1]

$$\%\text{R\_d} = (D_{\text{iw}} - D_{\text{fw}}) \times 100/D_{\text{iw}}, \tag{1}$$

where %R_d is the percentage of dust resuspended, D_{fw} is the final dust weight and D_{iw} is the initial dust weight.
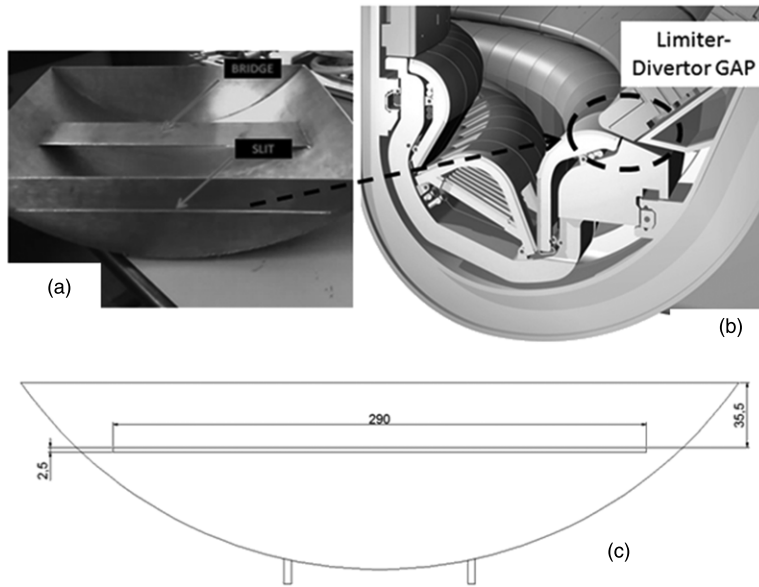
Figure 4. (*a*) The obstacle is placed in STARDUST to represent (*b*) the ITER divertor dome. The slit in (*a*) represents the limiter divertor gap in (*b*).
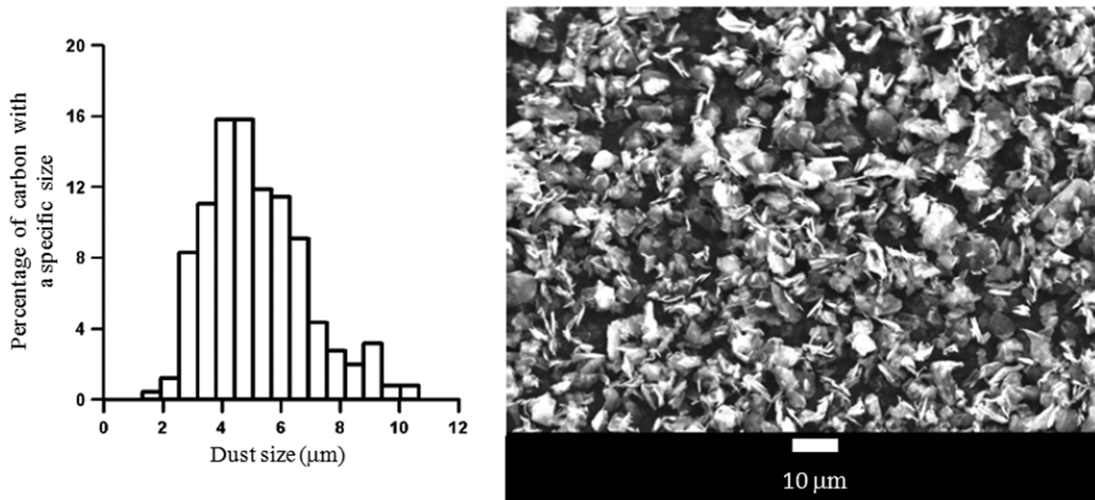

Figure 5. Left: distribution as a percentage of the sample versus size in micrometres. Right: SEM image of carbon dust [7].

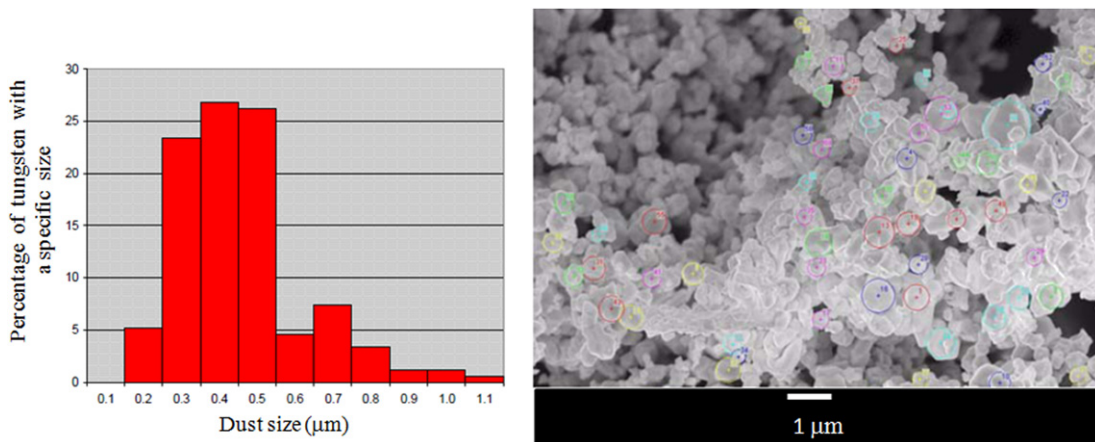**Figure 6.** Left: distribution as a percentage of the sample versus size in micrometres. Right: SEM image of tungsten dust [7].
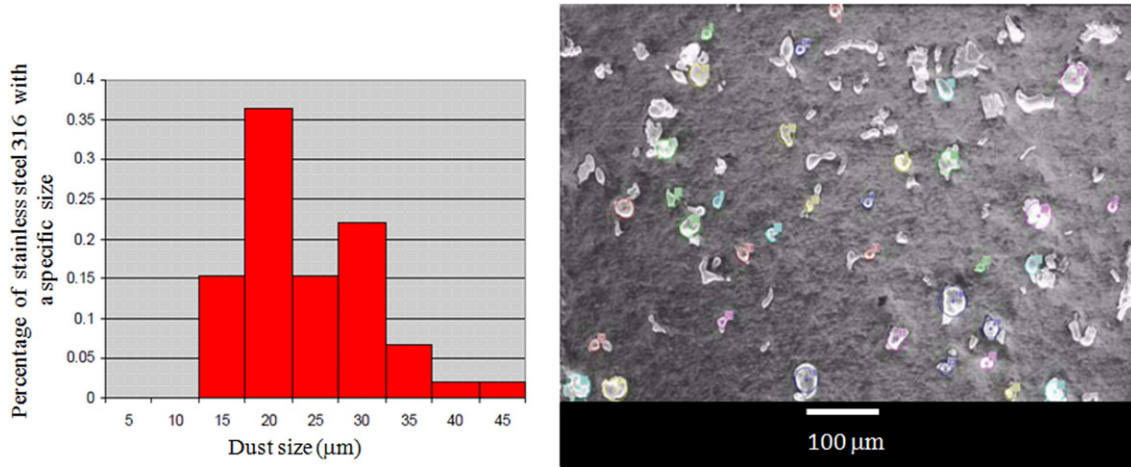
Figure 7. Left: distribution as a percentage of the sample versus size in micrometres. Right: SEM image of stainless steel 316 dust [7].
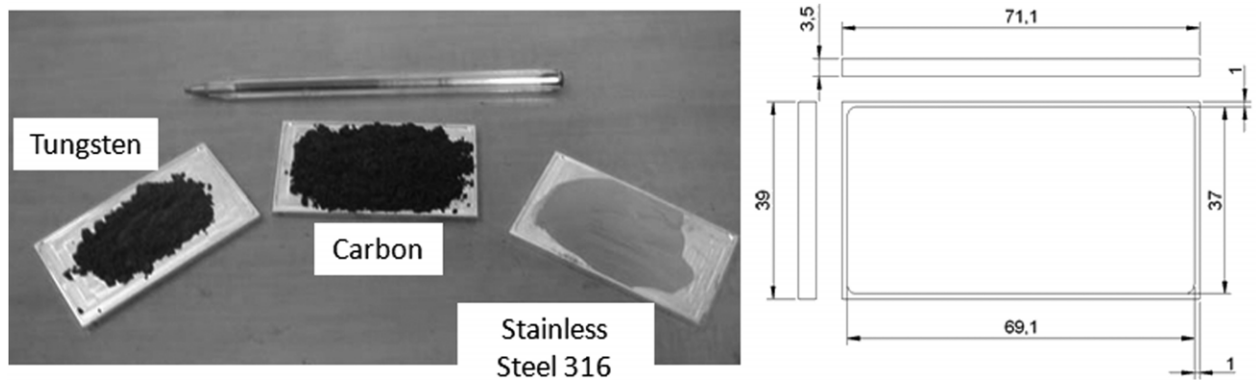

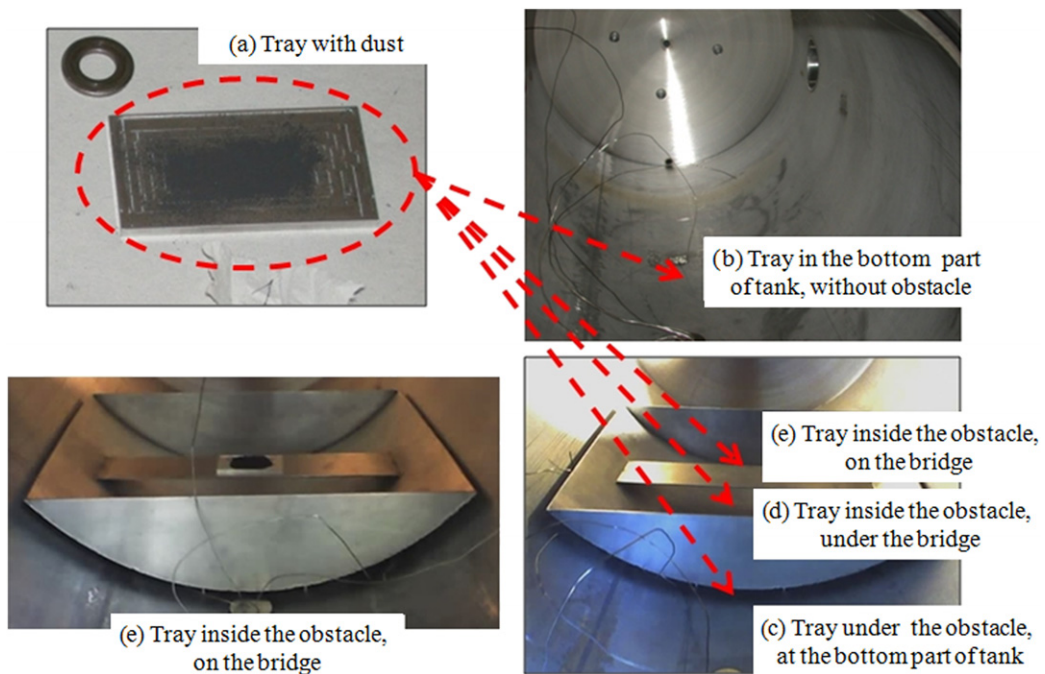**Figure 8.** Images of dust used and main dimensions of tray (in mm) [7].

Figure 9. STARDUST: different positions of the tray.

Table 1. Experimental results.

			1	2	3	4
		Tray position	No obstacle (110 °C)	Obstacle no slit (110 °C)	Obstacle no slit (25 °C)	Obstacle with slit (110 °C)
Tungsten test						
Mean mobilized fraction Valve B	a	Bottom of the tank	16.6%			
	b	Under obstacle		13.1%	14.8%	
	c	Under bridge		0.8%	0.1%	0.3%
	d	Over bridge		0.4%	0.1%	0.1%
Mean mobilized fraction Valve A	a	Bottom of the tank	0.2%			
	b	Under obstacle		0.2%	0%	
	c	Under bridge		0.1%	0.1%	0.2%
	d	Over bridge		0.2%	0.1%	0.2%
Stainless steel 316 test						
Mean mobilized fraction Valve B	a	Bottom of the tank	100%			
	b	Under obstacle		96.3%	99.1%	
	c	Under bridge		0.5%		0%
	d	Over bridge		0.4%	0%	0%
Mean mobilized fraction Valve A	a	Bottom of the tank	0.1%			
	b	Under obstacle		0.1%	0%	
	c	Under bridge		1.2%		0%
	d	Over bridge		0.3%	0%	0.1%
Carbon test						
Mean mobilized fraction valve B	A	Bottom of the tank	100%			
	B	Under obstacle		96.8%	98.4%	
	C	Under bridge		1.1%		0.1%
	d	Over bridge		0.7%	0.2%	0%
Mean mobilized fraction Valve A	a	Bottom of the tank	1.1%			
	b	Under obstacle		0.6%	0.1%	
	c	Under bridge		1.0%		0.1%
	d	Over bridge		0.8%	0.1%	0.1%

The weight of the dust has been measured by an electronic balance (precision 10^{-5} g).

3.2. Experimental results

The set of experiments with the tray inside the obstacle was carried out also with the slit on the obstacle. Every set of experiments has been repeated four times. Table 1 shows the mean fraction of dust mobilized, obtained for each different experimental set-up. These results are also summarized by the graphs in figure 10 (ordered per increasing amount of dust resuspended). The pressurization rate simulated in each experiment was set to 300 Pa s^{-1}.

The only noteworthy experimental results are those in which the dust tray was at the bottom of the tank. All the other tests gave negligible results from the mobilization point of view: as a matter of fact maximum 1% of the total amount of initial dust was mobilized. Figure 11 shows that the obstacle causes a slight diminution of mobilized dust for all three types of dust. It is more evident (about 4%) for SS316 and C at 110 °C, when the tray is placed under the obstacle. When the obstacle is placed inside the tank, a negligible increase in resuspended dust was noted in the case of cold experiments (at 25 °C), probably due to the fact that the dust tends to agglomerate because of the higher humidity at low temperatures or to the higher density of the carrier gas, in addition to the expected experimental 10% error in every weight of the dust, from which the mean value used in the comparisons is calculated. The presence of the slit in the

obstacle wall does not play any significant role in the dust resuspension. The expected increase, due to the two fluxes arriving on the tray from the valve directly and from the slit, was not confirmed. In contrast, if we take into account the slight variations noted in figures 12 and 13, as an example, and we suppose they are not in the measure error range, the slit seems to lower the mobilization effect. It is credible that the slit presence increases the turbulence and then reduces the velocity.

When the tray is placed under the bridge the maximum amount of mobilized dust is up to 1% when the air inlet is at the divertor port level (valve B) (figure 12). The slit seems to always play a negative effect on the dust mobilization. The same experimental evidence can be seen also in figure 13, with inlet from valve A and tray over the bridge. As said before, the mobilization is negligible under these two conditions.

4. Velocity field simulation

In order to study the relation between velocity and dust mobilization fraction a set of simulations have been carried out using the CFD code FLUENT [10], based on the finite volume method.

4.1. Introduction

FLUENT, a commercially available CFD solver together with the GAMBIT mesh generator (preprocessor), was used to simulate the flow behaviour in the same scenarios used
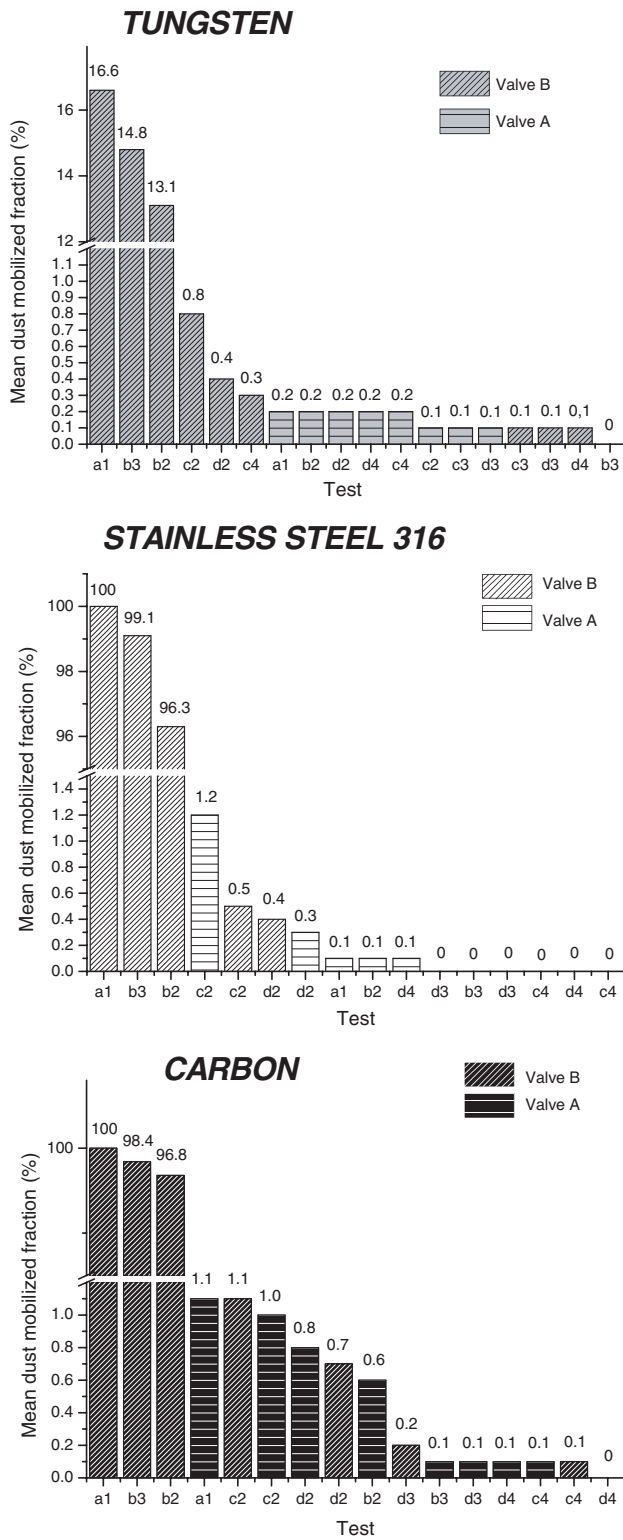
Figure 10. Mobilization fraction for each kind of dust per increasing amount of dust resuspended for each of the tests in table 1.

Figure 11. Percentage of resuspended dust, air inlet from valve B and tray at the bottom of the tank for the tests a1, b2 and b3 from table 1.

during the laboratory tests. The results of these simulations were visualized using the post-processing capabilities of FLUENT. For validation purposes, the CFD simulation data were extracted at the same locations where the experimental data were collected.
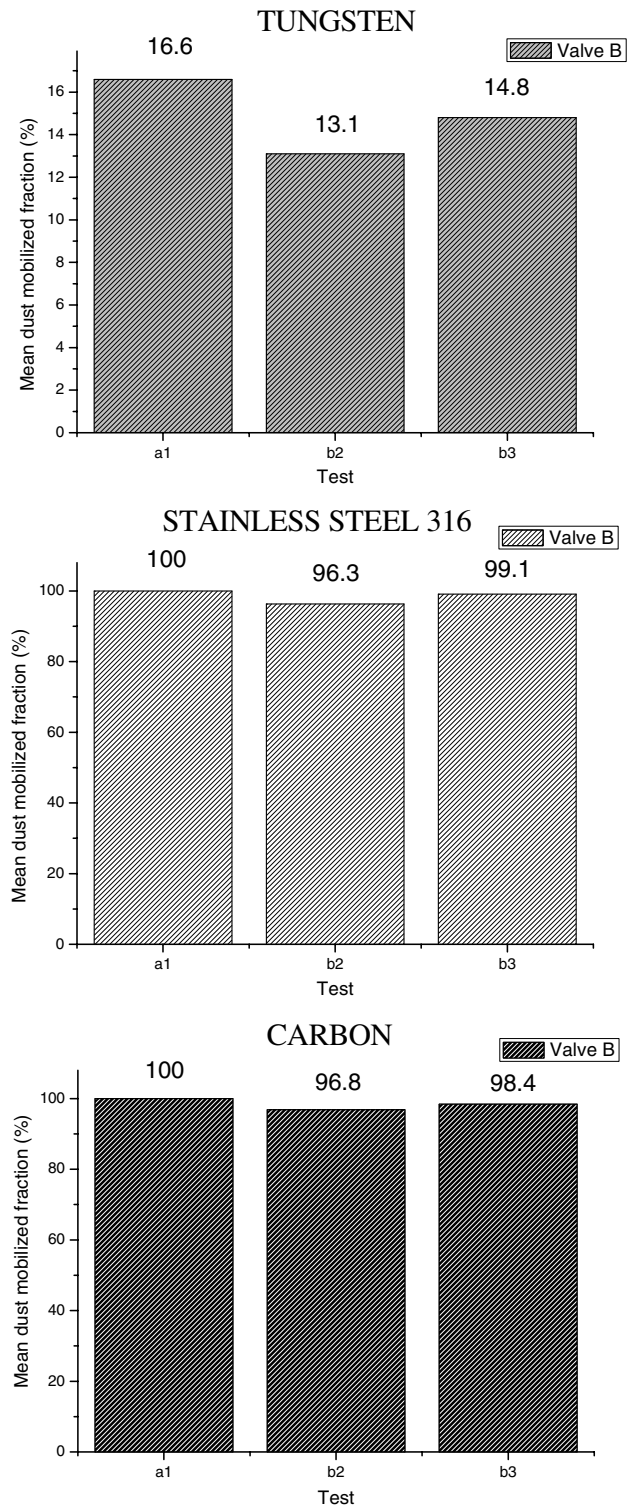
4.2. Governing equations and thermodynamic models

Nomenclature

- x, y, z: coordinated axis
- p: static pressure (Pa)
- $\vec{v}$: velocity vector (m s^{-1})

Figure 12. Influence of the slit on the resuspension for tests c2 and c4 of table 1. The inlet is valve B, the tray is under the bridge and the temperature $T = 110\,^{\circ}\text{C}$. Going from left to right, tungsten, stainless and carbon are shown as pairs for each test.
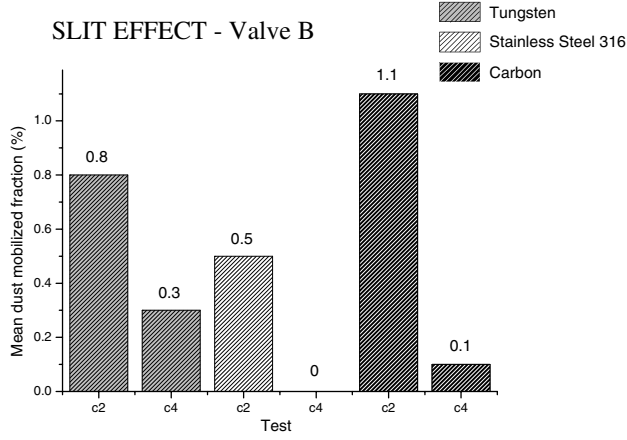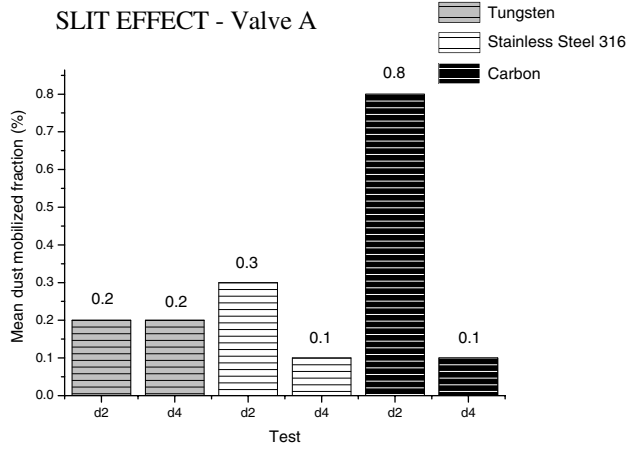

Figure 13. Influence of the slit on the resuspension for tests d2 and d4 of table 1. The inlet is valve B, the tray is under the bridge and the temperature $T = 110\,^{\circ}\text{C}$. Going from left to right, tungsten, stainless and carbon are shown as pairs for each test.

- u_i: component of velocity vector
- ρ: density
- S_m: source term
- μ: molecular viscosity (Pa s)
- $\rho\vec{g}$: gravitational body force
- $\vec{F}$: external body force vector (N m^{-3}) that arise from interaction with the dispersed phase
- I: unit tensor
- $\overline{\overline{\tau}}_{\text{eff}}$: stress tensor.

The implemented fluid-dynamic model is based on the fully compressible formulation of the continuity equation (2) and the momentum equation (3) (gravity effects are included):

$$\frac{\partial p}{\partial t} + \nabla \cdot (\rho \vec{v}) = S_m, \tag{2}$$

$$\frac{\partial}{\partial t}(\rho \vec{v}) + \nabla \cdot (\rho \vec{v} \vec{v})$$
$$= -\nabla p + \nabla \cdot \mu \left[(\nabla \vec{v} + (\nabla \vec{v}))^T - \frac{2}{3} \nabla \cdot \vec{v} I \right] + \rho \vec{g} + \vec{F}. \tag{3}$$

Turbulence is a main key for LOVA events. The RNG-based k–ε model, proposed for this specific application in a previous work [11], has been chosen because of its robustness and wide spread use. It improves the accuracy for rapidly strained flows compared with the standard k–ε model.

$$\frac{\partial}{\partial t}(\rho k) + \frac{\partial}{\partial x_i}(\rho k u_i) = \frac{\partial}{\partial x_j}\left(\alpha_k \mu_{\text{eff}} \frac{\partial k}{\partial x_j} \right)$$
$$+ G_{\text{k}} + G_{\text{b}} - \rho\varepsilon - Y_M + S_k. \tag{4}$$

$$\frac{\partial}{\partial t}(\rho \varepsilon) + \frac{\partial}{\partial x_i}(\rho \varepsilon u_i) = \frac{\partial}{\partial x_j}\left(\alpha_\varepsilon \mu_{\text{eff}} \frac{\partial \varepsilon}{\partial x_j} \right)$$
$$+ C_{1\varepsilon}\frac{\varepsilon}{k}(G_{\text{k}} + C_{3\varepsilon}G_{\text{b}}) - C_{2\varepsilon}\rho\frac{\varepsilon^2}{k} - R_\varepsilon + S_\varepsilon. \tag{5}$$

In these equations (3), (4), G_{k} represents the generation of turbulence kinetic energy due to the mean velocity gradients, G_{b} is the generation of turbulence kinetic energy due to buoyancy, Y_{M} represents the contribution of the fluctuating dilatation in compressible turbulence to the overall dissipation rate. The quantities α_k and α_ε are the inverse effective Prandtl numbers for k and ε, respectively. S_k and S_ε are user-defined source terms. The model constants $C_{1\varepsilon}$, $C_{2\varepsilon}$ and $C_{3\varepsilon}$ have values derived analytically by the RNG theory. The RNG-based k–ε turbulence model is derived from the instantaneous Navier–Stokes equations, using a mathematical technique called 'renormalization group' (RNG) methods. The analytical derivation results in a model with constants different from those in the standard k–ε model, and additional terms and functions in the transport equations for k and ε. The additional terms in the ε equation are given by (6)

$$R_\varepsilon = \frac{C_\mu \rho \eta^3 (1 - \eta/\eta_0)}{1 + \beta \eta^3} \cdot \frac{\varepsilon^2}{k} \tag{6}$$

$$\eta \equiv S_k/\varepsilon; \qquad \eta_0 = 4.38; \qquad \beta = 0.012.$$

A more comprehensive description of RNG theory and its application to turbulence can be found in [12]. This model was developed to better handle low Re regions. In low flow regions, in the beginning of the LOVA event, the dissipation rate can become small and cause unrealistically high turbulent viscosities. RNG theory provides an analytically derived differential formula for effective viscosity that accounts for low-Reynolds-number effects. The turbulent viscosity is calculated as (7)

$$d\left(\frac{\rho^2 k}{\sqrt{\varepsilon\mu}} \right) = \frac{1.72 \hat{v} d\hat{v}}{\sqrt{\hat{v}^3 + C_v - 1}} \tag{7}$$

where μ is again the molecular viscosity, C_v is a constant and $\hat{v}$ is the ratio of the sum between turbulent and molecular viscosity (effective viscosity) to molecular viscosity (8).

$$\hat{v} = \frac{\mu_{\text{eff}}}{\mu} = \frac{\mu_{\text{t}} + \mu}{\mu}; \qquad C_v \approx 100; \qquad \mu_{\text{t}} = \rho C_\mu \frac{k^2}{\varepsilon} \tag{8}$$

where C_μ is an empirical constant. Therefore, the turbulence will vary with the eddy scale. Effective use of this feature does, however, depend on an appropriate treatment of the near-wall region. In our case an enhanced wall treatment, with near wall refinement, has been chosen. It combines a two-layer model

with enhanced wall functions. The two-layer approach is used to specify both ε and the turbulent viscosity in the near-wall cells. In this approach, the whole domain is subdivided into a viscosity-affected region and a fully turbulent region. In the fully turbulent region the RNG-based k–ε model is employed. In the viscosity-affected near-wall region the one-equation model of Wolfstein [13] is employed. The demarcation of the two regions is determined by a wall-distance-based, turbulent Reynolds number (9)

$$Re_y \equiv \frac{\rho y \sqrt{k}}{\mu}, \qquad (9)$$

where y is the wall-normal distance calculated at the cell centres. The two-layer formulation for turbulent viscosity is used as a part of the enhanced wall treatment, in which the two-layer definition is smoothly blended with the high-Reynolds-number μ_t definition from the outer region, as proposed by Jongen [14]. To have a method that can extend its applicability throughout the near-wall region (i.e. viscous sublayer, buffer region and fully turbulent outer region) it is necessary to formulate the law of the wall as a single wall law for the entire wall region. The code achieves this by blending the logarithmic (turbulent) laws-of-the-wall using a function suggested by Kader [15]. This approach allows the fully turbulent law to be easily modified and extended to take into account other effects such as pressure gradients or variable properties. The enhanced turbulent law of the wall for compressible flow with heat transfer and pressure gradients has been derived by combining the approaches of White and Cristoph [16] and Huang *et al* [17]. The production of turbulence kinetic energy is computed using the velocity gradients that are consistent with the enhanced law of the wall ensuring a formulation that is valid throughout the near-wall region.

The implemented CFD model solves the energy equation (10) in the following form

$$\frac{\partial}{\partial t}(\rho E) + \nabla \cdot (\vec{v}(\rho E + p)) = \nabla \cdot (k_{\text{eff}} \nabla T + (\overline{\overline{\tau}}_{\text{eff}} \cdot \vec{v})) + S_{\text{h}} \qquad (10)$$

where k_{eff} is the effective conductivity and S_{h} is the source term. Heat transfer has been modelled using the Reynolds analogy, but for the RNG model, the effective thermal conductivity used in the energy equation is $k_{\text{eff}} = \alpha c_p \mu_{\text{eff}}$ where α (inverse of the turbulent Prandtl number) is calculated from (11)

$$\left|\frac{\alpha - 1.3929}{\alpha_0 - 1.3929}\right|^{0.6321} \left|\frac{\alpha - 2.3929}{\alpha_0 - 2.3929}\right|^{0.3679} = \frac{\mu}{\mu_{\text{eff}}} \qquad (11)$$

with $\alpha_0 = i/Pr = k/\mu c_p$.

Therefore, the turbulent Prandtl number is not constant as in the standard k–ε model, but it depends on the molecular Prandtl number. Developed analyses have been conducted in the transitory regime with an real gas assumption according to the Aungier–Redlich–Kwong (ARK) real gas model [18]. The ARK model was utilized to take into account the real gas behaviour at low temperature that is supposed to be present at the expansion zone due to the high pressure gradient (280 000– 100 Pa). The experimental evidence of these temperatures will be the object of future works. Thermo-physical properties of air are assumed to be varying with the kinetic theory assumption.

4.3. Numerical schemes and parameters

Simulations have been carried out in 2D, with a virtual third dimension, density-based solver in a unsteady formulation available in FLUENT. A third-order MUSCL discretization scheme has been used for momentum, turbulent kinetic energy, turbulent dissipation rate and energy. Gradients are estimated by the Green–Gauss node based method. The solution process is iterative and a convergence criterion is required. Convergence was assumed for each time step as all residuals fall until reaching a stable minimum, below 10^{-10}.

While time steps of 0.02 s would have been sufficient in order to account for the transient and compare the simulation with the experimental data, convergence concerns implied using a time step no greater than 1×10^{-5} s in all simulations.

4.4. Computational grid, initial data and boundary conditions

The geometry of the computational model has been created using the Gambit® software. For the discretization of the overall domain, 59 056 quadrilateral cells have been adopted. An important feature when discretizing the computational domain is to have a sufficient refinement along the direction of velocity gradient, namely normal at the inlet section in our case. Grid independence is an important stage in CFD modelling. Grid independence was achieved using a solution adaptive refinement, as cells can be added where they are needed in the mesh. The initial grid was adapted by putting more cells in the areas where the density gradient is higher than a chosen level. This process was repeated until the results became grid independent. Figure 14 shows three 2D meshes: mesh at 0.4s of 48 649 cells, mesh at 2s of 55 432 cells and mesh at 4s of 219 709 cells.

The last one shown above supplied reasonable performances in terms of CPU time. A mesh boundary layer was also considered on the wall of the model so that the mesh density can be increased to sufficiently resolve the boundary layer, without substantially increasing the total number of nodes. The boundary layer has been created dynamically by wall refinement in order to improve the performance of the mesh. In the k–ε based model, we need to specify the turbulence length scale as well as the turbulence intensity. Typical value of the turbulence intensity is chosen to be between 5% and 10%. There is no noticeable difference in the results if the turbulence intensity is varied in the range. In table 2 the turbulence parameters specified at the inlet section are shown.

When the enhanced wall treatment is employed the distance between the near-wall cell centroid and the wall, usually measured in the dimensionless wall units y^+, should be on the order $1 < y^+ < 5$. About the adopted discretization, the performed mesh shows wall y^+ values in accordance with the values foreseen by the theory for the turbulence model. A commonly used set-up of boundary conditions was configured. The gas inlet was taken as a mass-flow inlet with an inlet function given in figure 15.

Figure 15 shows that the inlet function used in the simulations follows the same trend of the experimental function obtained by the fit of the mass-flow inlet mean values acquired in every single experiment. The trend of the mass-flow inlet is not linear due to the fact that the flow meter
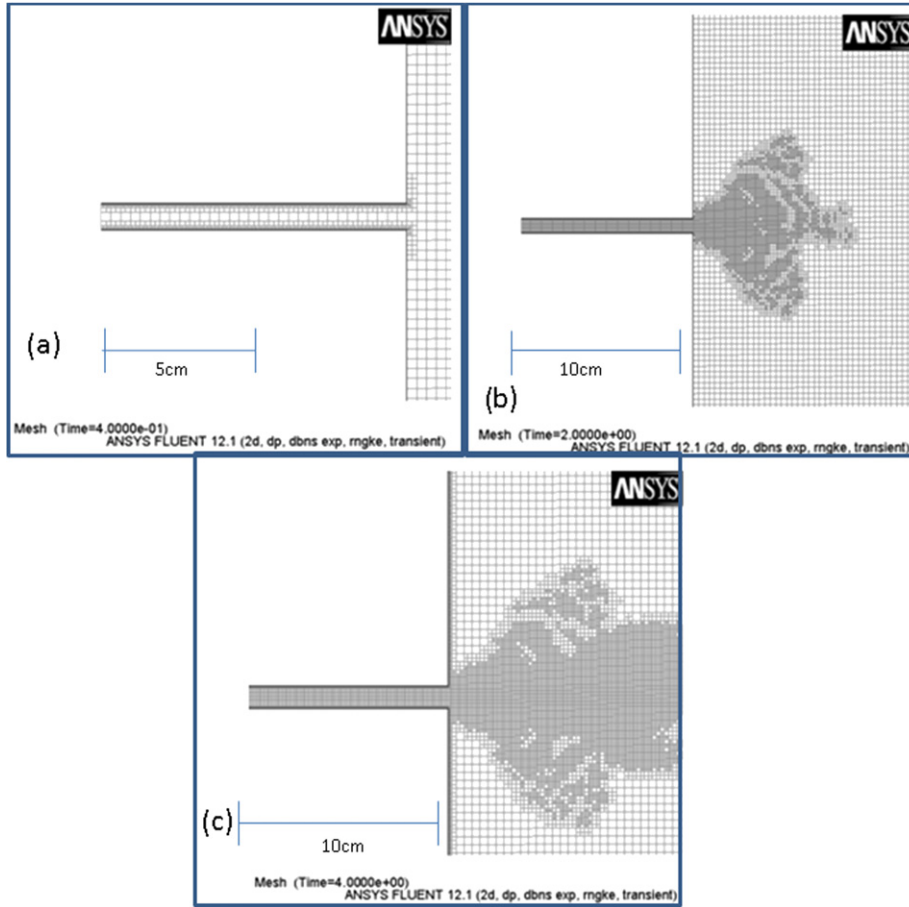
Figure 14. Mesh 2D with grid adaptation for inlet A at (*a*) 0.4 s, (*b*) 2 s and (*c*) 4 s.

Table 2. Turbulence parameters.

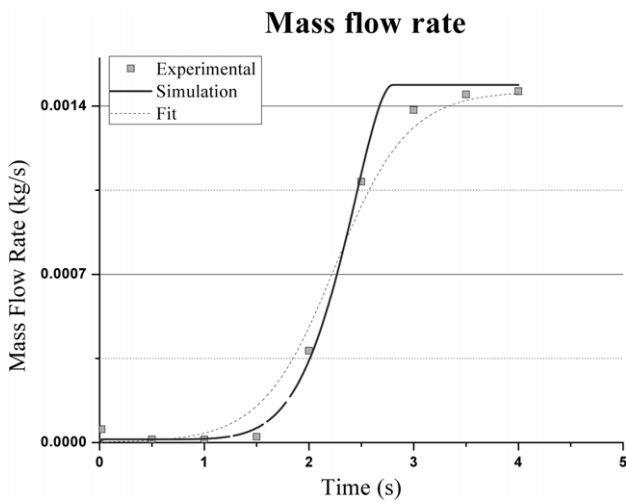| Turbulence parameters (k–ε RNG)	
Turbulence intensity	5%
Turbulence length scale (mm)	0.63

Figure 15. Mass flow rate (kg s^{-1}) versus time (s): For experimental (squares), numerical simulation (solid) and fit to experiment (dashed).
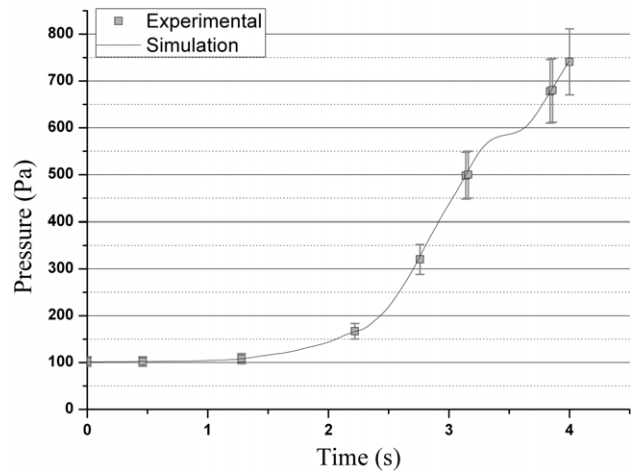

Figure 16. Pressure (Pa) versus time (s): For experimental (squares) and numerical simulation (solid).

needs about 3 s to reach the regime and guarantee the required 300 Pa s^{-1}. In figure 16 is shown the experimental static pressure function, calculated by the mean of the static pressure functions for every single experiment, compared with the simulated static pressure.
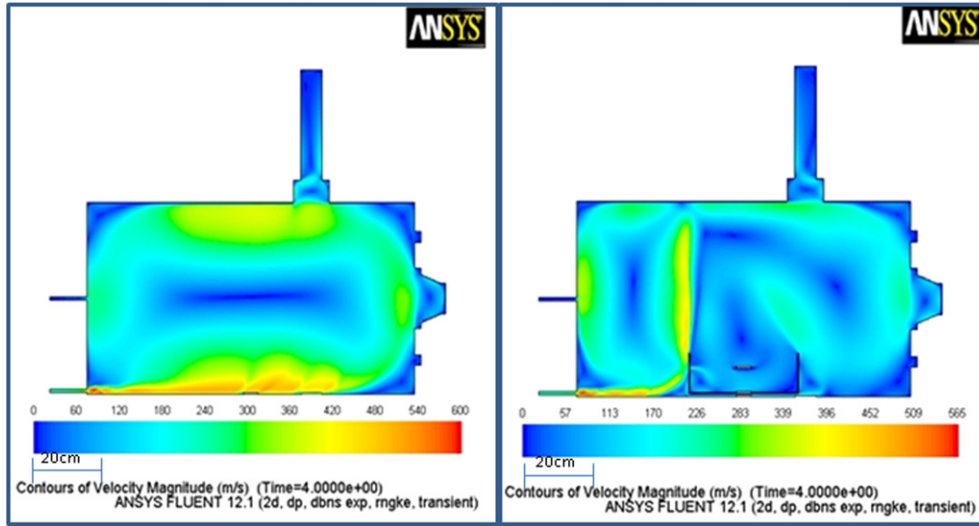
Figure 17. Velocity magnitude (inlet B without and with obstacle, blue–red is 0–600 m s^{-1} on the left and 0–566 m s^{-1} on the right).

Table 3. Velocity magnitude at 2 s for different positions.

	Tray position	No obstacle (25 °C)	Obstacle no slit (25 °C)	Obstacle with slit (25 °C)	No obstacle (110 °C)	Obstacle no slit (110 °C)	Obstacle with slit (110 °C)
Velocity magnitude Inlet valve A (m s^{-1})	Over bridge		69.2	68.5		90.1	89.2
	Under bridge		32.8	32.9		44.8	44.9
	Under obstacle		131.2	131.7		163.3	164.0
	Bottom of the tank	150.9			187.8		
Velocity magnitude Inlet valve B (m s^{-1})	Over bridge		30.1	29.6		39.2	38.5
	Under bridge		59.2	59.1		86.2	73.6
	Under obstacle		147.6	147.8		201.3	201.6
	Bottom of the tank	385			413.6		

The pressurization results carried out by the numerical simulation are in good agreement with the experimental data. No-slip conditions for fluid–solid interaction are set at the solid bounds of the fluid domain. Adiabatic conditions are applied to the lids and 110 °C or 25 °C test temperature conditions are applied at the lateral walls.

4.5. Numerical results

The actual computation time taken for solving a 4 s transient, using the 2D turbulent model with enhanced wall treatment, is 72 h. For our study this is a significant flow time because most dust mobilization phenomena occur in about 2 s, as it is possible to visualize through the glass window in STARDUST. The computations were performed using the CFD software on a AMD Phenom 9600 Quad Core with 8 GB of memory and a maximum speed of 2.26 GHz. The model which could predict the velocity during a LOVA event in the whole domain is an important tool to support model dust transport phenomena. Figure 17 illustrates the velocity magnitude in the whole domain at the end of simulation.

The maximum velocity is about 600 m s^{-1}. At the end of the inlet tube an expanding airflow with Mach number $M = 3$–3.66 (for different tests) is realized.
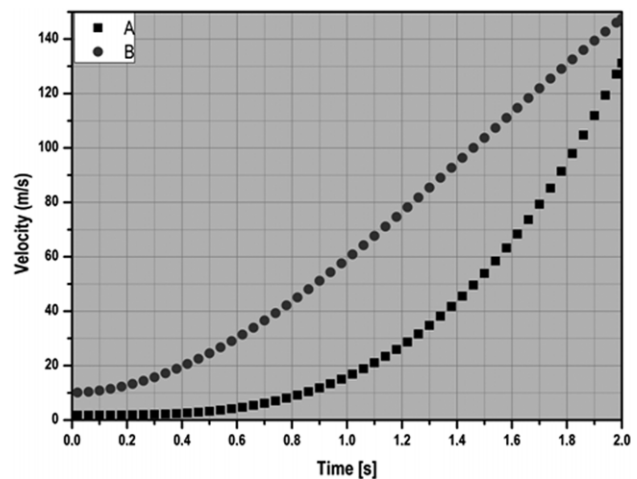

Figure 18. Numerical velocity (m s^{-1}) under obstacle versus time (s) using valve A (square) and valve B (circle).

It was shown that dust mobilization fraction may change from 100%, if an air stream that enters the VV directly hits the dust sample, to well below 1%, if the air stream is entering far from the dust location. The velocity results in table 3 can
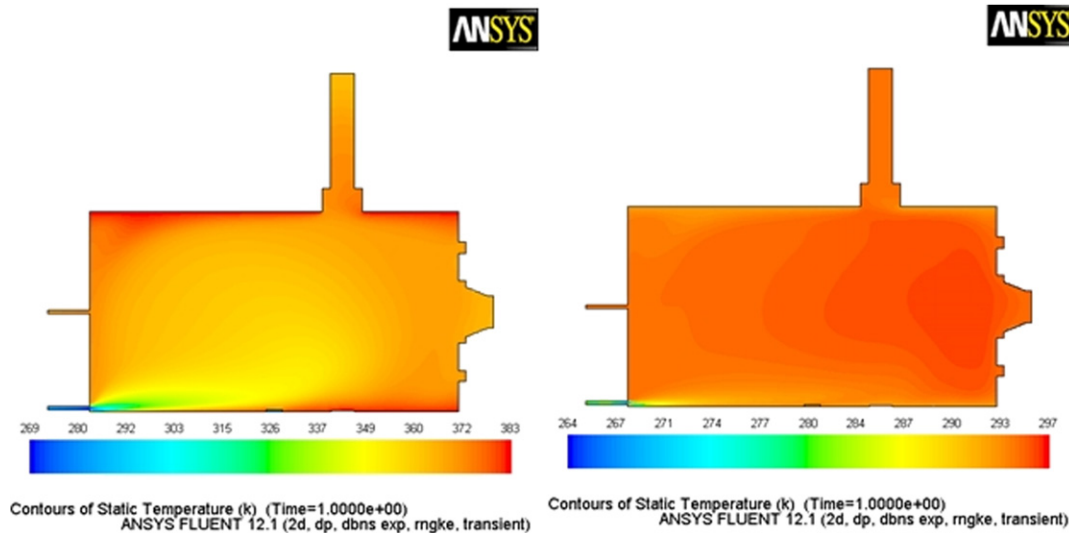
Figure 19. Temperature field for hot (left) wall and cold (right) transient (inlet B without obstacle, blue–red is 269–383 K on the left and 264–297 K on the right).

Table 4. Stokes numbers.

	SS316	Carbon	Tungsten
Mean particle diameter (μm)	25	4.5	0.4
Particle density (kg m^{-3})	8000	2267	19250
Stokes number	23.68	0.21	0.016

support the mobilization rate only for the experiments without obstacle. In fact, in this case the difference in the velocity between air inlet from valves A and B (from 150–188 m s^{-1} to 385–413 m s^{-1}) is consistent with the mobilization from 1% in the first case to 100% in the second one. The velocity curves relating to the cases in which the obstacle is inside the tank are shown in figure 18. It is evident that the differences in the velocity values between air inlet from valves A and B do not justify the differences in the mobilization.

These results suggest that the nodelization of the zone under the obstacle needs additional refinement, to fit better the mobilization data. The experimental data of the velocity taken in this critical zone are the key point to resolve this issue.

Figure 19 shows the temperature field, for both 110 and 25 °C test.

In this study, our concerns are primarily focused on modelling the turbulent flows; detailed dispersion and deposition patterns of particles are not studied. However, we tried to simulate particle paths only as a crude prediction of the dispersion of particles under turbulence. We cannot yet solve for the particle trajectories with a density-based solver and a real gas model, so we look at massless particle paths in the flow. This assumption, namely particles will follow the fluid streamlines closely, is true only for carbon and tungsten because the Stokes number was evaluated under the inlet section flow conditions (table 4).

These tracer particles are released from the inlet because of the constraints of the software usable by the numerical solver. The particle paths are shown in figure 20.

Although the flow pattern is very important in determining the dispersion and deposition of particles, the particle motion would naturally depend on physical characteristics of the dust,

such as their physical dimensions, electric and hygroscopic properties.

5. Discussion

A simulated low pressurization rate (300 Pa s^{-1}) LOVA event in ITER due to a small air leakage for two different positions of the leak, at the equatorial port level and at the divertor port level, has been carried out in order to evaluate the influence of obstacles, such as the divertor cassettes, and temperature on dust resuspension during both maintenance and accident conditions. To take into account the ITER VV wall conditions of temperatures during operation, the external walls of STARDUST were heated up to 110 °C. In another set of experiments the temperature was set to 25 °C, which represents the condition during maintenance. All the experimental conditions have been simulated to analyse the thermo-fluid dynamics behaviour inside STARDUST in the case of a LOVA. In this section the correspondence between the variation of velocity magnitude, provided by the simulations, and the relative dust mobilization for different characteristic points, in order to better understand how different VV conditions may influence the mobilization of the dust in the case of a LOVA, is discussed. The correspondence is guaranteed by the Stokes number only for tungsten and carbon.

5.1. Obstacle influence in dust mobilization

The experimental results obtained at an assigned temperature, for both valves A and B, show a slight reduction in resuspended dust when the tray is placed under the obstacle. Hence it is possible to state that the divertor causes the diminution of mobilized dust for W and C for a LOVA reproduction from both the equatorial and the divertor port level. The effect of the obstacle on the mobilization, i.e. the reduction in the resuspension due to the divertor, is shown in figure 21 for both valves A and B.

In every case there is a reduction of the mobilization related to the reduction in the velocity magnitude. Figure 21
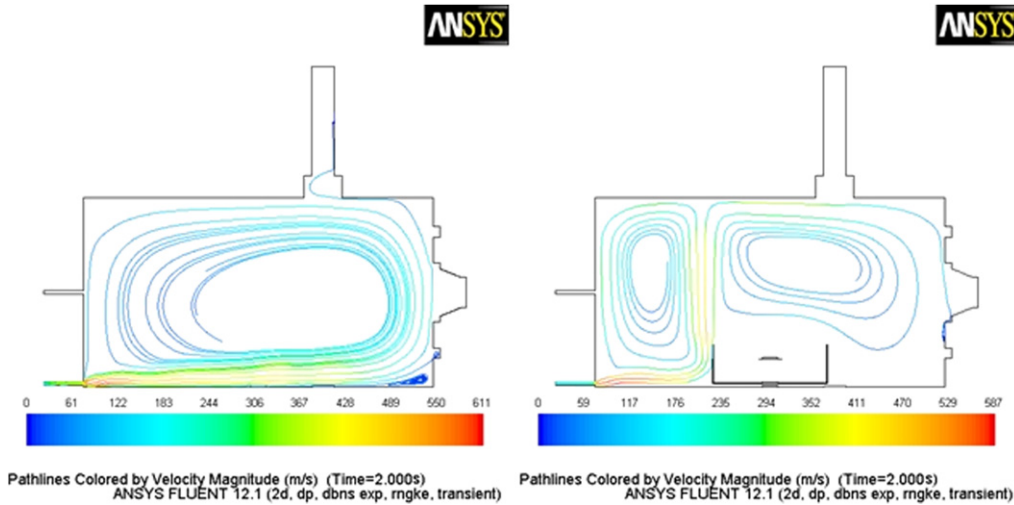
Figure 20. Pathlines of the particles without (left) and with (right) obstacle (inlet B, blue–red is 0–611 m s^{-1} on the left and 0–587 m s^{-1} on the right).

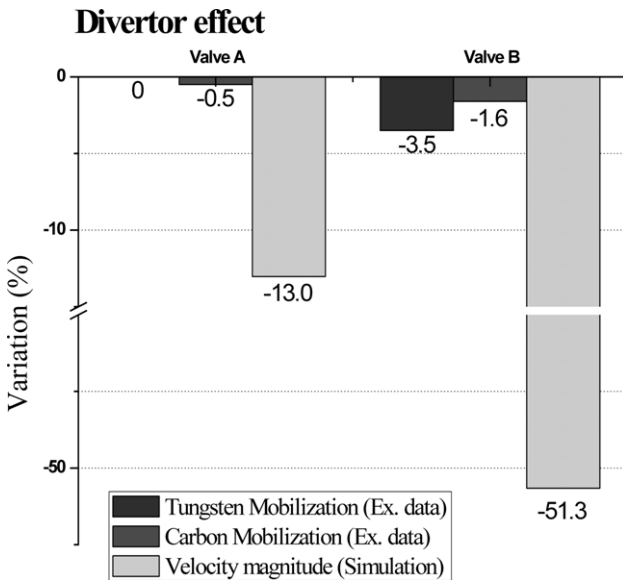**Figure 21.** Effect of the divertor: comparison between experimental dust mobilization and simulated velocity magnitude at $T_{wall} = 110\,°C$.

also shows the bigger influence of the divertor on the mobilization and the velocity, when a LOVA occurs from divertor port level.

5.2. Temperature influence in dust mobilization

The experimental results obtained at different temperatures (at 25 and at 110 °C) show for valve B a reduction in resuspended dust when the temperature increases. The effect of the temperature is shown in figure 22 for valve B.

The effects of the temperature on the dust mobilization are reported for valve B only, because this is the experimental configuration that gives the most significant results.

In the case of a LOVA occurring during operative conditions, the mobilization is lower than under maintenance conditions. Two factors can play a role for this behaviour:
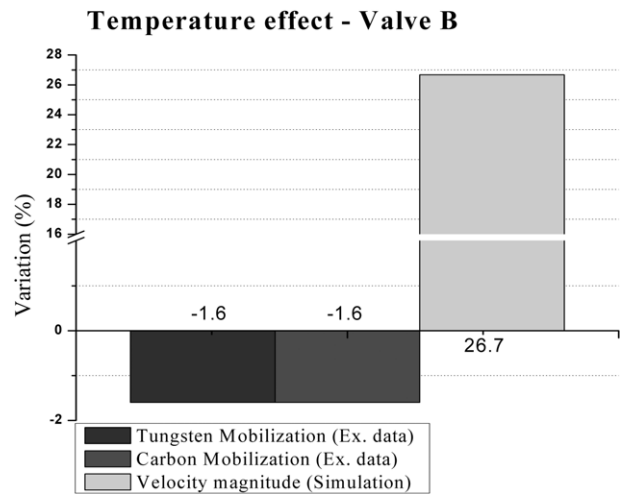

Figure 22. Effect of the temperature on dust mobilization for valve B: comparison between the percentage variation of dust mobilized (for tungsten and carbon) and the percentage variation of simulated velocity, calculated passing from a STARDUST 25 °C to 110 °C wall temperature.

the higher relative humidity value at lower temperature (that will be measured in future experimental campaigns) that may influence the dust agglomeration properties, causing the increase in the air-dust impact surface and the higher density of air.

5.3. Slit influence in dust mobilization

If a slit is applied on the obstacle at the bridge level, the experimental results, obtained at a assigned temperature, show a reduction in resuspended dust when the tray is placed:

- over the bridge, in the case the air inlet is from valve A;

and

- under the bridge, in the case the air inlet is from valve B.

The effect of the slit is shown in figure 23(*a*) for valve A and in figure 23(*b*) for valve B.
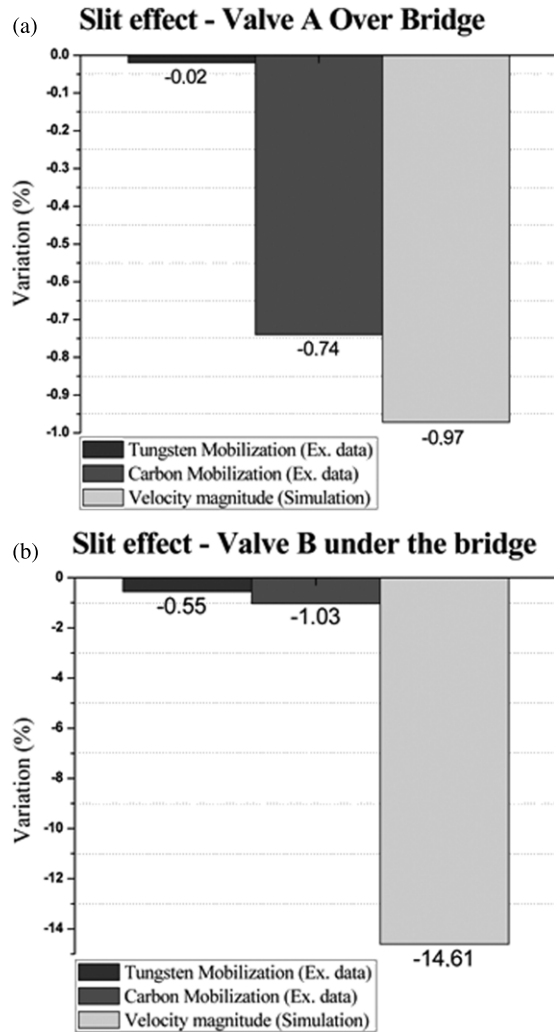
(a)
Slit effect - Valve A Over Bridge

Variation (%)

-0.02

-0.74

-0.97

- Tungsten Mobilization (Ex. data)
- Carbon Mobilization (Ex. data)
- Velocity magnitude (Simulation)

(b)
Slit effect - Valve B under the bridge

Variation (%)

-0.55 -1.03

-14.61

- Tungsten Mobilization (Ex. data)
- Carbon Mobilization (Ex. data)
- Velocity magnitude (Simulation)

Figure 23. (*a*). Effect of the slit for valve A, tray over the bridge, $T_{wall} = 110\,°C$ comparison between the percentage variation of dust mobilized (for tungsten and carbon) and the percentage variation of simulated velocity, calculated passing from the obstacle configuration without slit to the obstacle configuration with slit. (*b*) Effect of the slit for valve B, tray under the bridge, $T_{wall} = 110\,°C$ comparison between the percentage variation of dust mobilized (for tungsten and carbon) and the percentage variation of simulated velocity, calculated passing from the obstacle configuration without slit to the obstacle configuration with slit.

The limiter–divertor gap seems to have a negative effect on the dust mobilization. The local turbulence effect appears to play an important role in this reduction as shown in numerical results. The effect is more evident with carbon dust.

Cautions is necessary in the data interpretation because of the errors that could affect the measurements.

6. Conclusion

A certain amount of research concerning dust resuspension has been conducted in the USA and Japan.

In the USA (with the facility TDMX) experiments and simulations have been conducted to understand the behaviour of dust in the case of LOVA under dry conditions, obtaining no significant results [19].

The behaviour of dust in the case of LOVA under wet condition has been analysed in Japan [20] by measuring the influence of relative humidity influence on the dust resuspension.

Our research group focused on the influences of obstacle, temperature and limiter–divertor gap on dust resuspension and means of STARDUST facility that simulated a low pressurization rate ($300\,Pa\,s^{-1}$) LOVA event in ITER due to a small air leakage for two different positions of the leak, at the equatorial port level and at the divertor port level.

For the experiments done with the dust inside the tank (with and without obstacle) the most important evidence was:

- For both dusts used and for both valves there is a reduction of the mobilization related to the reduction in the velocity magnitude;
- The presence of an obstacle inside the STARDUST tank does not change significantly the dust mobilization rate obtained in the previous experimental campaigns using an empty tank [2];
- The higher temperature conditions play a slight positive role in reducing dust mobilization.
- The limiter–divertor gap seems to have a negative effect on the dust mobilization. The local turbulence effect appears to play an important role in this reduction.

In order to confirm this experimental evidence a two-dimensional (2D) modelling of STARDUST, made using the CFD commercial code FLUENT, was developed. For validation purposes the CFD simulation data were extracted at the same locations as the experimental data were collected. The simulations showed that the velocity is one of the driving parameters of the mobilization phenomena and coherent results have been obtained between calculated velocity and experimental resuspension rate in the tests without obstacle. Further analysis will be developed by including dust in numerical model in order to study particle properties influence.

The cases in which the obstacle is simulated need a more accurate study to achieve better agreement between the data. To achieve a strong experimental basis in supporting calculation a campaign of velocity acquisition data is on-going in STARDUST.

In conclusion, the boundary conditions to be used in the numerical model were taken from the experiments, so the comparison between numerical and experimental data was successfully completed and a first 2D CFD numerical model was developed.

The most important future developments will be:

- Image acquisition with a fast camera will be implemented in order to better understand the dust behaviour inside STARDUST;
- Using the 2D model to better analyse a shape for the new experimental facility (STARDUST Upgrade) in order to avoid the wall effects of the lids and to obtain a resuspension rate comparable to that expected in ITER. It will be achieved by rotating valves A and B as shown in figure 24.
- The experimental measurements of the low temperatures that are supposed to be present at the expansion zone due to the high pressure gradient (280 000 to 100 Pa) will be the object of future works;
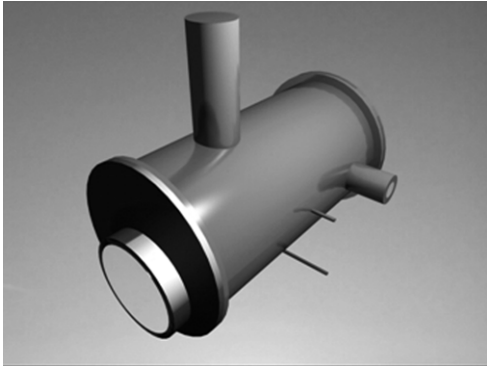
Figure 24. STARDUST Upgrade: it will be achieved by rotating valves A and B in order to avoid the wall effects of the lids and to obtain a resuspension rate comparable to that expected in ITER.

- Construction of a multiphase model in order to simulate dust behaviour and resuspension phenomena

The aim of this work and its future developments is to obtain experimental results in order to benchmark mechanistic models that can subsequently be applied to any scale.

References

[1] Bellecci C., Gaudio P., Lupelli I., Malizia A., Porfiri M.T. and Richetta M. 2008 Dust mobilization and transport measures in the STARDUST facility *EPS2008: Proc. 35th EPS Conf. on Plasma Physics (Hersonissos, Crete, 9–13 June 2008)* vol 32 (ECA) p P-1.175 And http://epsppd.epfl.ch/Hersonissos/pdf/P1_175.pdf

[2] Porfiri M.T., Forgione N., Paci S. and Rufoloni A. 2006 Dust mobilization experiments in the context of the fusion plants—STARDUST facility *Fusion Eng. Des.* **81** 1353–8

[3] Eberta E. and Raeder J. 1991 LOCA, LOFA and LOVA analyses pertaining to NET/ITER safety design guidance *Fusion Eng. Des.* **17** 307–12

[4] ITER-JCT 2001 *Generic Site Safety Report* N84 Garching, Germany

[5] Van Dorsselaere J.P., Perrault D., Barrachin M., Bentaib A., Bez J., Cortès P., Seropian C., Trégourès N. and Vendel J. 2009 R&D on support to ITER safety assessment *Fusion Eng. Des.* **84** 1905–11

[6] Porfiri M.T., Libera S., Paci S., Rufoloni A. and Verdini L. 2003 StarDust facility: first series of the tungsten dust mobilization experiments *ENEA FUS-TN-SA-SE-R-83*, Frascati, Italy

[7] Porfiri M.T., Forgione N., Frediani F., Libera S., Paci S., Rufoloni A. and Verdini L. 2003 StarDust facility: dust mobilization experiments *ENEA FUS-TN-SA-SE-R-94*, Frascati, Italy

[8] Koizumi K. *et al* 1998 Design and development of the ITER vacuum vessel *Fusion Eng. Des.* **41** 299–304

[9] Nakaharai H., Chuman T., Ebara S.,Yokomine T., Shimizu A. and Korenaga T. 2002 Entrainment behavior of activated dusts in the fusion reactor under LOVA *Fusion Eng. Des.* **63–64** 313–8

[10] FLUENT 6.2 User's Guide, January 2005

[11] Humrickhouse P.W., Sharpe J.P. and Corradini M.L. 2007 Modeling of the toroidal dust mobilization experiment *Fusion Sci. Technol.* **52** 1022–6

[12] Zhang Y. and Orszag S.A. 1986 Renormalization group analysis of turbulence: I. Basic theory *J. Sci. Comput.* **1** 3–51

[13] Wolfstein M. 1969 The velocity and temperature distribution of one-dimensional flow with turbulence augmentation and pressure gradient *Int. J. Heat Mass Transfer* **12** 301–18

[14] Jongen T. 1992 Simulation and modeling of turbulent incompressible flows *PhD Thesis* EPF Lausanne, Lausanne, Switzerland

[15] Kader B. 1981 Temperature and concentration profiles in fully turbulent boundary layers *Int. J. Heat Mass Transfer* **24** 1541–4

[16] White F. and Christoph G. 1971 A simple new analysis of compressible turbulent skin friction under arbitrary conditions *Technical Report* AFFDL-TR-70-133

[17] Huang P., Bradshaw P. and Coakley T. 1993 Skin friction and velocity profile family for compressible turbulent boundary layers *AIAA J.* **31** 1600–4

[18] Johnson R.W. 1998 *The Handbook of Fluid Dynamics* (Cambridge: Cambridge University Press)

[19] Sharpe J.P. and Humrickhouse P.W. 2006 Dust mobilization studies in the TDMX facility *Fusion Eng. Des.* **81** 1409–15

[20] Matsuki K., Suzuki S., Ebara S., Yokomine T. and Shimizu A. 2006 Dust mobilization by high-speed vapor flow under LOVA *Fusion Eng. Des.* **81** 1347–51